Lattice relaxation and energy band modulation in twisted bilayer graphene

Nguyen N. T. Nam[1] and Mikito Koshino[2]

[1]*Department of Physics, Tohoku University, Sendai 980-8578, Japan*
[2]*Department of Physics, Osaka University, Toyonaka 560-0043, Japan*
(Received 13 June 2017; published 28 August 2017)

We theoretically study the lattice relaxation in the twisted bilayer graphene (TBG) and its effect on the electronic band structure. We develop an effective continuum theory to describe the lattice relaxation in general TBGs and obtain the optimized structure to minimize the total energy. At small rotation angles $<2°$, in particular, we find that the relaxed lattice drastically reduces the area of the AA stacking region and forms a triangular domain structure with alternating AB and BA stacking regions. We then investigate the effect of the domain formation on the electronic band structure. The most notable change from the nonrelaxed model is that an energy gap of up to 20 meV opens at the superlattice subband edges on the electron and hole sides. We also find that the lattice relaxation significantly enhances the Fermi velocity, which was strongly suppressed in the nonrelaxed model.

I. INTRODUCTION

Twisted bilayer graphene (TBG) is a two-dimensional material where two graphene layers are relatively rotated by an arbitrary angle. Such a rotational stacking structure has been widely observed in epitaxially grown multilayer graphenes [1–7] and also it can be fabricated by manually aligning single layers using the transfer technique [8,9]. The electronic properties of TBG have also been intensively studied in theory, where it was shown that the energy spectrum sensitively depends on its rotation angle θ [10–21]. In a small θ, in particular, the interference between the incommensurate lattice structures gives rise to a moiré pattern with a long spacial period, and it significantly influences the low-energy spectrum. For TBG less than a few degrees, in particular, the Dirac cones of the two layers are strongly hybridized by the moiré interlayer interaction, where the linear dispersion is distorted into superlattice subbands [10–21]. The characteristic features of superlattice band structure of TBG were actually observed in recent experiments [22–24].

Most of the band calculations for TBG assumes that the two graphene layers are rigid and simply stacked without changing the original honeycomb lattices. In a real system, however, the lattice structure spontaneously relaxes to achieve an energetically favorable structure [25–29], and it should influence the electronic spectrum. If we consider a TBG with a small rotation angle as in Fig. 1, for instance, we notice that the lattice structure locally resembles the regular stacking such as AA, AB, BA, or saddle point (SP), depending on the position. Here AA represents the perfect overlapping of hexagons, while AB and BA are shifted configurations in which the A(B) sublattice is right above B(A). Since the interlayer binding energy is the lowest in AB and BA and the highest in AA stacking [25,30,31], the TBG spontaneously deforms so as to maximize the AB/BA areas while minimizing the AA area. In fact, such an AB/BA domain structure was experimentally observed in multilayer graphenes grown by chemical vapor deposition [32–34]. In theory, the lattice relaxation in TBG was computationally studied by the density functional (DFT) calculation [26], molecular dynamics [27], the structural optimization with DFT-based empirical potential

[29], and also by the hybrid continuum model combined with DFT parametrization [28], while its implication of the domain formation on the electronic band structure is still unclear. Similar lattice relaxation was also found in another moiré superlattice of graphene on hexagonal boron nitride [35–40], where the sublattice inequality in hBN results in a hexagonal domain pattern [41–44].

In this work, we present a theoretical study on the lattice relaxation in TBG and its effect on the electronic band structure. First, we develop a minimum phenomenological model to describe the AB/BA domain formation in TBGs with general angles. Using the elastic theory and a simple interlayer adhesion potential, we express the total energy as a functional of the lattice deformation $\mathbf{u}(\mathbf{r})$ and optimize it by solving the Euler-Lagrange equation. In decreasing the rotation angle θ, we actually find that $\mathbf{u}(\mathbf{r})$ increases and eventually forms a sharp domain structure with AB and BA regions clearly separated into a triangular pattern.

We then investigate the effect of the domain formation on the electronic spectrum of TBG. The lattice distortion is expected to affect the band structure by modifying the moiré pattern, and also by adding the strain-induced vector potential to graphene's Dirac electron [45–47]. Here we calculate the band structure of relaxed TBGs by the tight-binding model and compared it with the nonrelaxed case. A significant difference is observed in $\theta < 2°$, where the domain structure becomes pronounced. The most notable effect is that an energy gap of up to 20 meV appears at the superlattice subband edge between the lowest and the second subband, while it was hardly found in the nonrelaxed model. We also find that the lattice deformation significantly enhances the Fermi velocity, which was strongly suppressed in the nonrelaxed model [15,48]. The associated lattice distortion induces the pseudomagnetic field more than 30 T, which alternates in space with the moiré superlattice period.

The paper is organized as follows. In Sec. II we introduce the lattice geometry of TBG and the description of the moiré pattern. In Sec. III, we develop the effective continuum theory for the lattice relaxation. First we consider the simpler one-dimensional model as an intuitive example, and then we extend the model to two-dimensional TBG. In Sec. IV, we calculate
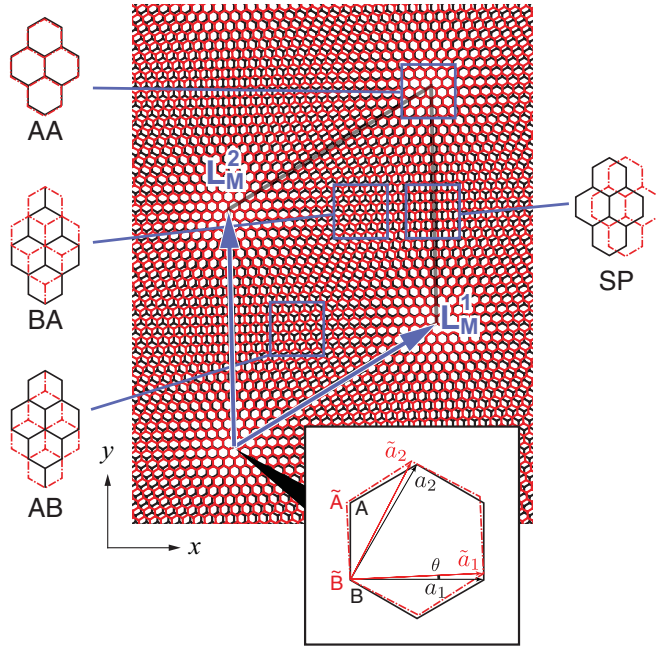
FIG. 1. Twisted bilayer graphene at rotation angle $\theta = 2.65°$. The blue squares indicate the regions where the lattice structure locally resembles a regular stacking arrangement such as AA, AB, BA, and SP (see the text). Parallelogram is the moiré unit cell.

the electronic band structure of relaxed TBGs and discuss the effect of the lattice deformation. A short conclusion is given in Sec. V.

II. GEOMETRY OF TWISTED BILAYER GRAPHENE

Let us consider a TBG lattice as illustrated in Fig. 1. Here we specify the stacking geometry by starting from the AA-stacking bilayer graphene and rotate layer 2 with angle θ with respect to layer 1. In Fig. 1, we take $\theta = 2.65°$ as an example. We define the primitive lattice vectors of layer 1 as $\mathbf{a}_1 = a(1,0)$, $\mathbf{a}_2 = a(1/2, \sqrt{3}/2)$, where $a = 0.246$ nm is graphene's lattice constant. The primitive lattice vectors of layer 2 can be obtained by rotating those of layer 1 as $\tilde{\mathbf{a}}_i = R(\theta)\mathbf{a}_i$ ($i = 1,2$), where $R(\theta)$ is rotation matrix. The reciprocal lattice vectors of layer 1 are given by $\mathbf{a}_1^* = 2\pi/a(1, -1/\sqrt{3})$ and $\mathbf{a}_2^* = 2\pi/a(0, 2/\sqrt{3})$, and those of layer 2 by $\tilde{\mathbf{a}}_i^* = R(\theta)\mathbf{a}_i^*$ ($i = 1,2$).

The Brillouin zones of layers 1 and 2 are shown in Fig. 2 by two large black, red dashed hexagons, respectively. In TBG, they are folded into reduced Brillouin zones shown by small blue hexagons. We label the corner points of the folded Brillouin zone by $\bar{K}$ and $\bar{K}'$, the midpoint of each side by $\bar{M}$, and the zone center by $\bar{\Gamma}$.

When the rotation angle is small, the mismatch of the lattice periods of two rotated layers gives rise to the long-period moiré beating pattern, of which the spatial period is estimated as follows. In the rotation from the AA stacking, an atom on layer 2 originally located at site $\mathbf{r}_0$ (right above the layer 1's atom) is moved to the new position $\mathbf{r} = R(\theta)\mathbf{r}_0$. Then we define the interlayer atomic shift $\boldsymbol{\delta}(\mathbf{r})$ as the in-plane position of an layer 2's atom at $\mathbf{r}$ measured from its counterpart on
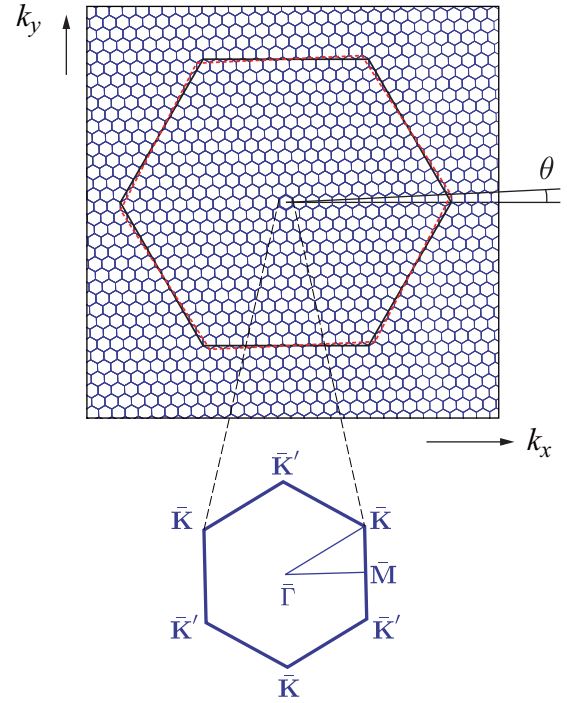

FIG. 2. Brillouin zones of layer 1 (black hexagon), layer 2 (red dashed hexagon), and twisted bilayer graphene (blue hexagons) at $\theta = 2.65°$.

layer 1, i.e.,

$$\boldsymbol{\delta}(\mathbf{r}) = \mathbf{r} - \mathbf{r}_0 = (1 - R^{-1})\mathbf{r}. \tag{1}$$

When $\boldsymbol{\delta}(\mathbf{r})$ coincides with a lattice vector of layer 1, then the position $\mathbf{r}$ (layer 2's atom) is occupied also by an atom of layer 1, so that the local lattice structure at $\mathbf{r}$ takes AA arrangement as in the origin. Therefore, the primitive lattice vector of the moiré superlattice $\mathbf{L}_i^{\mathrm{M}}$ is obtained from the condition $\boldsymbol{\delta}(\mathbf{L}_i^{\mathrm{M}}) = \mathbf{a}_i$, which leads to

$$\mathbf{L}_i^{\mathrm{M}} = (1 - R^{-1})^{-1}\mathbf{a}_i \quad (i = 1,2). \tag{2}$$

The lattice constant $L_{\mathrm{M}} = |\mathbf{L}_1^{\mathrm{M}}| = |\mathbf{L}_2^{\mathrm{M}}|$ is given by

$$L_{\mathrm{M}} = \frac{a}{2\sin(\theta/2)}. \tag{3}$$

The corresponding moiré reciprocal lattice vectors satisfying $\mathbf{G}_i^{\mathrm{M}} \cdot \mathbf{L}_j^{\mathrm{M}} = 2\pi\delta_{ij}$ are written as

$$\mathbf{G}_i^{\mathrm{M}} = (1 - R)\mathbf{a}_i^* = \mathbf{a}_i^* - \tilde{\mathbf{a}}_i^* \quad (i = 1,2), \tag{4}$$

where we used $R^\dagger = R^{-1}$.

In general TBGs, the lattice structure is not exactly periodic in the atomic level, since the moiré interference pattern is not generally commensurate with the lattice period. However, the superlattice becomes rigorously periodic at some special θ, where vector $m\mathbf{a}_1 + n\mathbf{a}_2$ meets vector $n\mathbf{a}_1' + m\mathbf{a}_2'$ with certain integers m and n [11]. The exact superlattice period is then given by

$$L = |m\mathbf{a}_1 + n\mathbf{a}_2| = a\sqrt{m^2 + n^2 + mn} = \frac{|m - n|a}{2\sin(\theta/2)}, \tag{5}$$

which is $|m - n|$ times as big as the moiré period L_{M}. The rotation angle θ is equal to the angle between two lattice

TABLE I. Index (m,n), the rotation angle θ, the size of the moiré unit cell L_M, and the dimensionless parameter η (see Sec. III) for several TBGs considered in this paper.

(m,n)	$\theta[°]$	$L_M[\text{nm}]$	η
(12, 13)	2.65	5.33	0.258
(22, 23)	1.47	9.59	0.464
(27, 28)	1.20	11.72	0.567
(31, 32)	1.05	13.42	0.650
(33, 34)	0.987	14.27	0.691
(40, 41)	0.817	17.26	0.835
(60, 61)	0.547	25.78	1.248

vectors $m\mathbf{a}_1 + n\mathbf{a}_2$ and $n\mathbf{a}_1 + m\mathbf{a}_2$, and it is explicitly given by

$$\cos\theta = \frac{1}{2}\frac{m^2 + n^2 + 4mn}{m^2 + n^2 + mn}. \tag{6}$$

In Table I, we present (m,n), the rotation angle θ, the size of the moiré unit cell L_M, and the dimensionless parameter η (introduced in Sec. III) for several TBGs considered in this paper.

III. OPTIMIZED LATTICE STRUCTURE

A. 1D atomic chain

To describe the lattice relaxation in the continuum theory, we start with a one-dimensional (1D) model [25] as a simple and intuitive example. The extension to TBG is straightforward, as we will see in the next section. Here we consider a 1D moiré superlattice as shown in Fig. 3(a), which is composed of two atomic chains 1 and 2 having slightly different lattice periods, $a = L_M/N$ and $a' = L_M/(N-1)$, respectively, with a large integer N. The common period of the whole system is given by L_M. Inside a supercell, there are N sites and $N-1$ sites in chains 1 and 2, respectively. This model can be viewed as an interacting two-chain version of the Frenkel-Kontorova model.

In TBG, the atoms in different layers can be associated by rotation. Likewise, the atoms of chains 1 and 2 are associated by expansion. We can then define the interchain atomic shift $\delta(x)$ as the relative position of the site on chain 2 located at x measured from the position of its counterpart on chain 1, or

$$\delta(x) = x - \frac{N-1}{N}x = \frac{a}{L_M}x. \tag{7}$$

This corresponds to Eq. (1) in TBG. Obviously we have $\delta(nL_M) = na$ for integer n, i.e., the atoms on different chains are vertically aligned at $x = nL_M$.

Now we introduce the attractive interaction between the atoms of chains 1 and 2, while allowing the atoms to move only parallel to the chain. We expect that the atoms move their positions to reduce the interchain binding energy U_B. As a result, the system tends to increase the vertically aligned region, and then a domain structure should be formed as schematically illustrated in Fig. 3(b). At the same time, however, such deformation increases the elastic energy U_E, so the optimized state can be obtained by minimizing the total energy $U = U_E + U_B$.
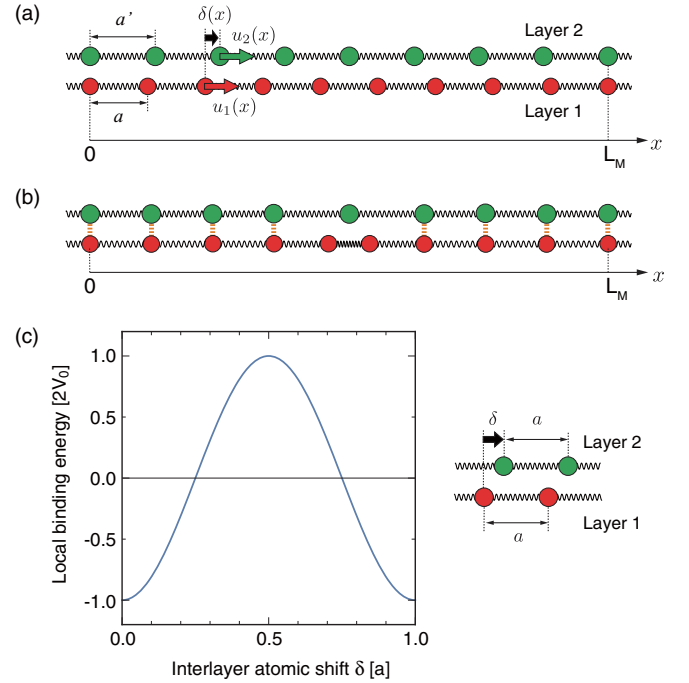

FIG. 3. (a) One-dimensional moiré superlattice model. (b) Schematic picture of the relaxed structure, where the atoms are locked to the vertically aligned positions, leaving a domain boundary in the middle. (c) Interlayer binding energy per length as a function of the relative translation δ for commensurate double chains.

Now we define $u_1(x)$ and $u_2(x)$ as a displacement of atomic positions on layers 1 and 2, respectively, measured from the nonrelaxed state. The interchain atomic shift in the presence of deformation is then

$$\delta(x) = \delta_0(x) + u_2(x) - u_1(x), \tag{8}$$

where $\delta_0(x) = (a/L_M)x$ is that in the absence of deformation, Eq. (7). Following the standard elastic theory, we assume that the elastic energy is expressed as

$$U_E = \int \frac{1}{2}\kappa\left[\left(\frac{\partial u_1}{\partial x}\right)^2 + \left(\frac{\partial u_2}{\partial x}\right)^2\right]dx, \tag{9}$$

where κ is an elastic constant to characterize the stiffness of the lattice.

If a is very close to a', the moiré superperiod L_M is much greater than the lattice constant a, and then the local lattice structure resembles commensurate chains with the identical lattice period a, which are relatively shifted by some specific δ [Fig. 3(c)]. Let define $V[\delta]$ as the interchain binding energy per unit length of the commensurate chains. Here we assume an attractive interaction described by the sinusoidal function for $V[\delta]$,

$$V[\delta] = -2V_0\cos a^*\delta, \tag{10}$$

where $V_0 > 0$ and $a^* = 2\pi/a$. Obviously $V[\delta]$ is periodic with period a, because the sliding by the lattice spacing a is equivalent to no sliding. It takes a minimum at the vertically aligned arrangement, $\delta = na$ (n: integer), and maximum at the half shift $\delta = (n + 1/2)a$. In the incommensurate chains in which a and a' are slightly different, the interchain

atomic shift δ is not a constant but slowly varies as a function of x. Therefore, the interchain binding energy of the incommensurate chains as a whole is written as

$$U_B = \int V[\delta(x)]dx. \tag{11}$$

By using Eqs. (7), (8), and (10), we have $V[\delta(x)] = -2V_0 \cos[G_M x + a^*(u_1 - u_2)]$, where $G_M = 2\pi/L_M$ is the reciprocal vector for the moiré superlattice, and we used the relation $a^*\delta_0(x) = G_M x$.

The total energy $U = U_B + U_E$ is a functional of $u_1(x)$ and $u_2(x)$. Here we define the coordinates $u_\pm = u_1 \pm u_2$ and rewrite U as a functional of $u_\pm$. The optimized state to minimize the total energy is obtained by solving the Euler-Lagrange equations,

$$\kappa \frac{\partial^2 u_+}{\partial x^2} = 0, \tag{12}$$

$$\kappa \frac{\partial^2 u_-}{\partial x^2} - 4a^* V_0 \sin(G_M x + a^* u_-) = 0. \tag{13}$$

In the following, we assume that the lattice deformation keeps the original superlattice period, i.e., $u_\pm(x)$ is periodic in x with period L_M. Then $u_+(x) = $ const. is the only solution of the first equation. To solve the second, we apply the Fourier transformation,

$$u_-(x) = \sum_n u_n e^{inG_M x}, \tag{14}$$

$$\sin(G_M x + a^* u_-(x)) = \sum_n f_n e^{inG_M x}. \tag{15}$$

Equation (13) is then reduced to

$$u_n = -\frac{4a^* V_0}{\kappa(nG_M)^2} f_n. \tag{16}$$

Equations (14)–(16) are a set of self-consistent equations to be solved.

By scaling the displacement $u_i(x)$ by a, Eq. (16) can be written in a dimensionless form,

$$\frac{u_n}{a} = -\frac{2\eta^2}{\pi n^2} f_n, \tag{17}$$

where η is a dimensionless parameter defined by

$$\eta = \sqrt{\frac{V_0}{\kappa}} \frac{L_M}{a}. \tag{18}$$

Roughly speaking, the parameter η characterizes how many harmonics are relevant in the displacement $u_-(x)$. Since f_n is of the order of 1, the condition that u_n is comparable to a is given by $2\eta^2/(\pi n^2) \gtrsim 1$, or

$$n \lesssim \sqrt{\frac{2}{\pi}} \eta. \tag{19}$$

When η is small such that $(2/\pi)^{1/2}\eta \ll 1$, only the first harmonic term is relevant so $u_-(x)$ is well approximated by a single sinusoidal function. This situation occurs in a stiff lattice (large κ), weak interchain interaction (small V_0), or small moiré period (small L_M). When η is large, on the contrary, the large number of harmonics is significant so that $u_-(x)$ becomes a sharp function with respect to the moiré period L_M.
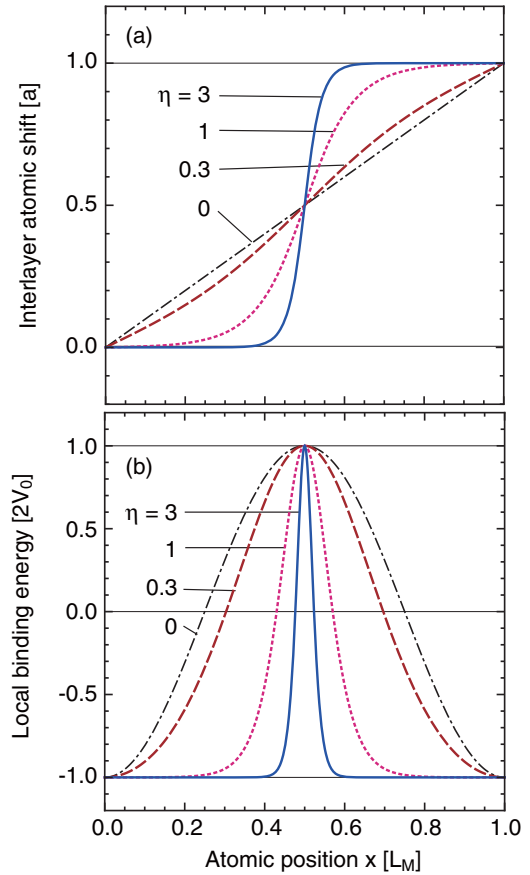

FIG. 4. (a) Interlayer atomic shift $\delta(x)$ and (b) local binding energy $V[\delta(x)]$ plotted against the position x in one-dimensional moiré superlattice with $\eta = 0$, 0.3, 1, and 3.

This condition corresponds to soft lattice, strong interaction, and large moiré period.

The self-consistent equations, Eqs. (14)–(16), can be solved by numerical iteration with higher harmonics appropriately truncated. In Fig. 4(a), we plot the interlayer atomic shift $\delta(x)$ for the optimized state at some different η's. The line of $\eta = 0$ represents the nonrelaxed case $\delta_0(x) = ax/L$, and the relative shift from this line represents the displacement $u_-(x)$. The actual displacement on each chain is given by $u_1 = -u_-/2$ and $u_2 = u_-/2$. At $\eta = 0.3$, u_- is small compared to the atomic spacing a, and it contains only low-frequency Fourier components. In increasing η, the u_- becomes larger and at the same time higher harmonics become more relevant. In $\eta = 3$, we clearly see a steplike structure consisting of two plateau regions of $\delta = 0$ and a, which are nothing but domains where the atoms are locked to the vertically aligned positions. Figure 4(b) presents the corresponding plot for the local binding energy $V[\delta(x)]$. We see that the original cosine function at $\eta = 0$ is gradually deformed so as to expand the plateau regions. In $\eta = 3$, the system achieves the minimum energy almost everywhere, except for a thin domain boundary in the middle.

Actually, the sharp domain boundary observed in large η is well approximated by an analytical soliton solution. If we concentrate on a small region near the domain boundary

centered at $x = L_M/2$, Eq. (13) is reduced to

$$\kappa \frac{\partial^2 u_-}{\partial x'^2} + 4a^* V_0 \sin(a^* u_-) = 0, \qquad (20)$$

where $x' = x - L_M/2$, and the term $G_M x$ is approximated by $G_M(L_M/2) = \pi$, assuming the domain boundary is much narrower compared to L_M. This has an exact solution [25]

$$u_-(x') = \frac{2a}{\pi} \arctan\left[\exp\left(4\pi\sqrt{\frac{V_0}{\kappa}}\frac{x'}{a}\right)\right] - \frac{a}{2}, \qquad (21)$$

which is found to nicely agree with the numerically obtained u_- near the boundary. Therefore, the typical width of the domain boundary is characterized by

$$w_d \approx \frac{a}{4}\sqrt{\frac{\kappa}{V_0}}. \qquad (22)$$

Using Eqs. (18) and (22), we have

$$\frac{w_d}{L_M} = \frac{1}{4\eta}, \qquad (23)$$

so the parameter η characterizes the ratio of the domain wall width to the moiré unit cell.

B. Twisted bilayer graphene

The above formulation for a 1D moiré superlattice can be extend to the TBG system in a straightforward manner. Let us consider a TBG with a long-period moiré pattern as illustrated in Fig. 1, and introduce the lattice deformation which is specified by the displacement vector $\mathbf{u}^{(l)}(\mathbf{r})$ for layer $l = 1,2$. The interlayer atomic shift under the deformation is then given by

$$\boldsymbol{\delta}(\mathbf{r}) = \boldsymbol{\delta}_0(\mathbf{r}) + \mathbf{u}^{(2)}(\mathbf{r}) - \mathbf{u}^{(1)}(\mathbf{r}), \qquad (24)$$

where $\boldsymbol{\delta}_0(\mathbf{r})$ is one without lattice deformation, which is defined by Eq. (1). Here we neglect the out-of plane component of the displacement vectors and concentrate on the in-plane motion in order to describe the domain formation within the simplest framework. The expected effect of the out-of-plane corrugation will be discussed later. The elastic energy is expressed by [43,45]

$$U_E = \sum_{l=1}^{2} \int \frac{1}{2}\left\{(\lambda + \mu)\left(u_{xx}^{(l)} + u_{yy}^{(l)}\right)^2\right.$$
$$\left. + \mu\left[\left(u_{xx}^{(l)} - u_{yy}^{(l)}\right)^2 + 4\left(u_{xy}^{(l)}\right)^2\right]\right\}d^2\mathbf{r}, \qquad (25)$$

where $S_M = (\sqrt{3}/2)L_M^2$ is the area of the moiré unit cell, $\lambda \approx 3.5$ eV/Å^2 and $\mu \approx 7.8$ eV/Å^2 are typical values graphene's Lamé factor [42], and $u_{ij}^{(l)} = (\partial_i u_j^{(l)} + \partial_j u_i^{(l)})/2$ is the strain tensor.

When the moiré superperiod L_M is much greater than the lattice constant a, the local lattice structure can be viewed as nonrotated bilayer graphene relatively shifted by $\boldsymbol{\delta}$ depending on the position (Fig. 5). We define as $V[\boldsymbol{\delta}]$ the interlayer binding energy per area of nonrotated bilayer graphene. In the simplest approximation, it can be written as a cosine
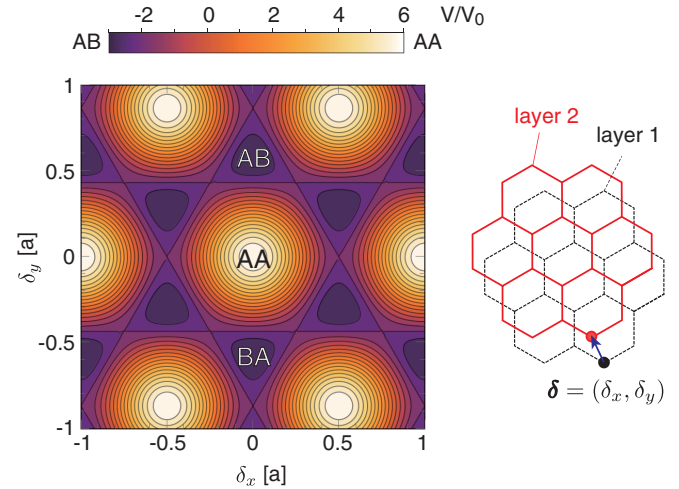

FIG. 5. Interlayer binding energy $V[\boldsymbol{\delta}]$ of TBG as a function of local atomic shift $\boldsymbol{\delta}(\mathbf{r})$.

function $\boldsymbol{\delta}$ as

$$V[\boldsymbol{\delta}] = \sum_{j=1}^{3} 2V_0 \cos[\mathbf{a}_j^* \cdot \boldsymbol{\delta}], \qquad (26)$$

where $\mathbf{a}_3^* = -\mathbf{a}_1^* - \mathbf{a}_2^*$. The function takes the maximum value $6V_0$ at AA stacking ($\boldsymbol{\delta} = 0$) and the minimum value $-3V_0$ at AB and BA stacking. The difference between the binding energies of AA and AB/BA structure is $9V_0$ per area, and this amounts to $\Delta\epsilon = 9V_0 S_G/4$ per atom, where S_G is the area of the graphene's unit cell. In the following calculation, we use $\Delta\epsilon = 0.0189$ (eV/atom) as a typical value [25,30]. The potential profile of $V[\boldsymbol{\delta}]$ is presented in Fig. 5.

In TBG, $\boldsymbol{\delta}$ is not a constant but slowly varying as a function of the 2D position. Then the interlayer binding energy of TBG as a whole is written as

$$U_B = \int V[\boldsymbol{\delta}(\mathbf{r})]d^2\mathbf{r}. \qquad (27)$$

$V[\boldsymbol{\delta}]$ is periodic in $\boldsymbol{\delta}$ with the lattice period of graphene. By using Eqs. (24) and (26), we have

$$V[\boldsymbol{\delta}(\mathbf{r})] = \sum_{j=1}^{3} 2V_0 \cos\left[\mathbf{G}_j^M \cdot \mathbf{r} + \mathbf{a}_j^*(\mathbf{u}^{(2)} - \mathbf{u}^{(1)})\right], \qquad (28)$$

where $\mathbf{G}_3^M = -\mathbf{G}_1^M - \mathbf{G}_2^M$ and we used the relation $\mathbf{a}_j^* \cdot \boldsymbol{\delta}_0(\mathbf{r}) = \mathbf{G}_j^M \cdot \mathbf{r}$.

In Eq. (27), U_B depends only on the local relative translation $\boldsymbol{\delta}(\mathbf{r})$, while the local rotation is neglected. This approximation is based on the fact that the local structure within an area of a few a (graphene lattice constant) resembles the nonrotated bilayer with translation $\boldsymbol{\delta}$. If we further consider the local rotation θ, each atomic position in the area is shifted by $r\theta$, where r is the radius of the rotation which has the scale of a few a. On the other hand, the translation $\boldsymbol{\delta}$ itself is of the order of a, so that $r\theta$ is much smaller than $\boldsymbol{\delta}$ when θ is small. As we see later, the local rotation angle in the low-angle TBGs considered in this work turns out to be no more than a few degrees, so that the local rotation effect can be safely neglected in U_B.

The relaxed state can be obtained by minimizing the total energy $U = U_E + U_B$ as a functional of $\mathbf{u}^{(l)}(\mathbf{r})$. We define $\mathbf{u}^{\pm} = \mathbf{u}^{(2)} \pm \mathbf{u}^{(1)}$ and rewrite U as a functional of $\mathbf{u}^{\pm}$. In the following we consider only $\mathbf{u}^{-}$, as we are interested in the relative displacement between atoms on two layers. The Euler-Lagrange equations for $\mathbf{u}^{-}$ read

$$\frac{1}{2}(\lambda + \mu)\left(\frac{\partial^2 u_x^-}{\partial x^2} + \frac{\partial^2 u_y^-}{\partial x \partial y}\right) + \frac{1}{2}\mu\left(\frac{\partial^2 u_x^-}{\partial x^2} + \frac{\partial^2 u_x^-}{\partial y^2}\right)$$

$$+ \sum_{j=1}^{3} 2V_0 \sin\left[\mathbf{G}_j^{\mathrm{M}} \cdot \mathbf{r} + \mathbf{a}_j^* \cdot \mathbf{u}^-\right] g_j^x = 0, \qquad (29)$$

$$\frac{1}{2}(\lambda + \mu)\left(\frac{\partial^2 u_y^-}{\partial y^2} + \frac{\partial^2 u_x^-}{\partial x \partial y}\right) + \frac{1}{2}\mu\left(\frac{\partial^2 u_y^-}{\partial x^2} + \frac{\partial^2 u_y^-}{\partial y^2}\right)$$

$$+ \sum_{j=1}^{3} 2V_0 \sin\left[\mathbf{G}_j^{\mathrm{M}} \cdot \mathbf{r} + \mathbf{a}_j^* \cdot \mathbf{u}^-\right] g_j^y = 0, \qquad (30)$$

We define the Fourier components $\mathbf{u}_\mathbf{q}^-$ and $f_\mathbf{q}^j (j = 1,2,3)$ as

$$\mathbf{u}^-(\mathbf{r}) = \sum_\mathbf{q} \mathbf{u}_\mathbf{q}^- e^{i\mathbf{q}\cdot\mathbf{r}}, \qquad (31)$$

$$\sin\left[\mathbf{G}_j^{\mathrm{M}} \cdot \mathbf{r} + \mathbf{a}_j^* \cdot \mathbf{u}^-(\mathbf{r})\right] = \sum_\mathbf{q} f_\mathbf{q}^j e^{i\mathbf{q}\cdot\mathbf{r}}, \qquad (32)$$

where $\mathbf{q} = m_1 \mathbf{G}_1^{\mathrm{M}} + m_2 \mathbf{G}_2^{\mathrm{M}}$ are vectors of the reciprocal superlattice. The Euler-Lagrange equations (29) and (30) are rewritten in a matrix form as

$$\mathbf{u}_\mathbf{q}^- = \sum_{j=1}^{3} 4V_0 f_\mathbf{q}^j \hat{K}_\mathbf{q}^{-1} \mathbf{a}_j^*,$$

$$\hat{K}_\mathbf{q} = \begin{pmatrix} (\lambda + 2\mu)q_x^2 + \mu q_y^2 & (\lambda + \mu)q_x q_y \\ (\lambda + \mu)q_x q_y & (\lambda + 2\mu)q_y^2 + \mu q_x^2 \end{pmatrix}. \qquad (33)$$

Equations (31)–(33) are a set of self-consistent equations. Following Eq. (18) in the 1D model, the number of the relevant harmonics in $\mathbf{u}_\mathbf{q}^-$ is roughly characterized by a dimensionless parameter

$$\eta = \sqrt{\frac{V_0}{\lambda + \mu}} \frac{L_{\mathrm{M}}}{a}. \qquad (34)$$

In TBG, we have two elastic constants λ and μ, and it is ambiguous which should replace the position of κ in Eq. (18) for the 1D model. Here we adopt the simple sum $\lambda + \mu$ in Eq. (34). Figure 6 plots η as a function of the rotation angle θ. The approximation with the lowest harmonics (i.e., six $\mathbf{q}$ points of $\pm \mathbf{G}_1^{\mathrm{M}}, \pm \mathbf{G}_2^{\mathrm{M}}, \pm \mathbf{G}_3^{\mathrm{M}}$) is valid when $\eta \ll 1$, or $\theta > \sim 2°$. The contribution of high-frequency harmonics is not negligible when η is of the order of 1.

We numerically solve the self-consistent equation for several TBGs by numerical iterations with a sufficiently large cutoff in q space. Some details in the calculation and obtained $\mathbf{u}_\mathbf{q}^-$ for several TBGs are presented in the Appendix. Figure 7 presents an example of the calculated result for lattice relaxation in $\theta = 1.05°$, where the central panel plots the displacement vector $\mathbf{u}^-(\mathbf{r})$ as a function of position, and the right three panels show the local atomic structure near AA,
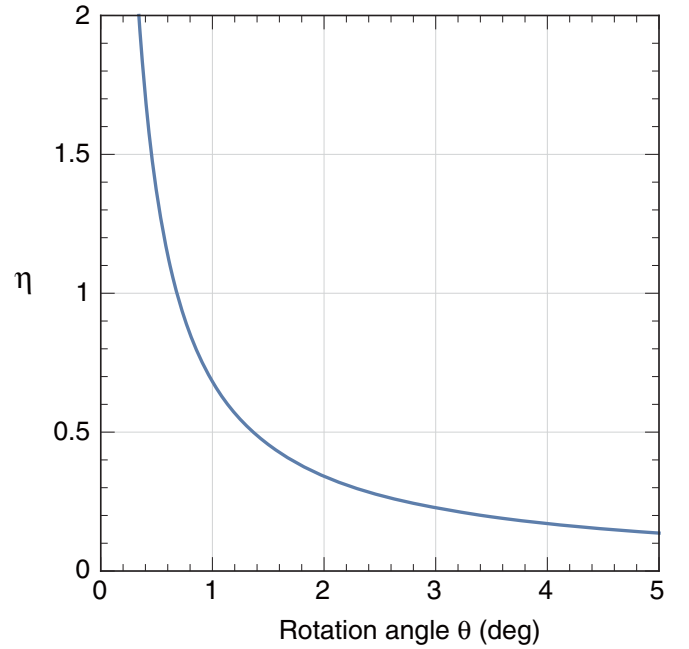

FIG. 6. Dimensionless parameter η as a function of rotation angle θ.

AB, and SP points before and after the relaxation. The actual displacement on each layer is given by $\mathbf{u}^{(1)} = -\mathbf{u}^-/2$ and $\mathbf{u}^{(2)} = \mathbf{u}^-/2$. We actually observe that the $\mathbf{u}^-$ rotates around the center of the AA region, where the local rotation angle between two layers is increased from $1.05°$ to $1.63°$. As a result, the AA region is significantly shrunk while the AB region is expanded.

Figure 8 summarizes the results for TBGs from $\theta = 2.65°$ down to $0.547°$. Here the panels in (a) show the absolute value of the displacement vector $\mathbf{u}^-(\mathbf{r})$ as a function of position. The distribution of $\mathbf{u}^-(\mathbf{r})$ on the two-dimensional place looks similar among all the cases, where it takes the maximum on a ringlike region near the AA spot. On the other hand, its magnitude strongly depends on θ, where the $|\mathbf{u}^-|$ is much smaller than the atomic scale a in $\eta \ll 1$, while it eventually becomes comparable when η is of the order of 1. Figure 8(b) presents the corresponding plots for the local binding energy $V[\boldsymbol{\delta}(\mathbf{r})]$. When $\mathbf{u}^-(\mathbf{r})$ is much smaller than a, as in $\theta = 2.65°$, the potential profile is approximately given by $V[\boldsymbol{\delta}_0(\mathbf{r})]$, which is essentially a sum of three plain waves. In decreasing θ, the spots of the AA regions shrink and AB and BA regions eventually dominate. The result looks especially dramatic in small angles less than $1°$, where the relaxed lattices clearly exhibit a triangular domain pattern of AB and BA regions. Similar to Eq. (22) for the 1D model, the characteristic width of the domain boundary is given by

$$w_{\mathrm{d}} \approx \frac{a}{4}\sqrt{\frac{\lambda + \mu}{V_0}} \approx 5.2 \text{ nm}. \qquad (35)$$

Indeed, it roughly agrees with the typical scale of the AB/BA domain wall in Fig. 8(b). It is also consistent with the experimental observation of the shear boundary, which estimates the averaged width about 6 nm [34].
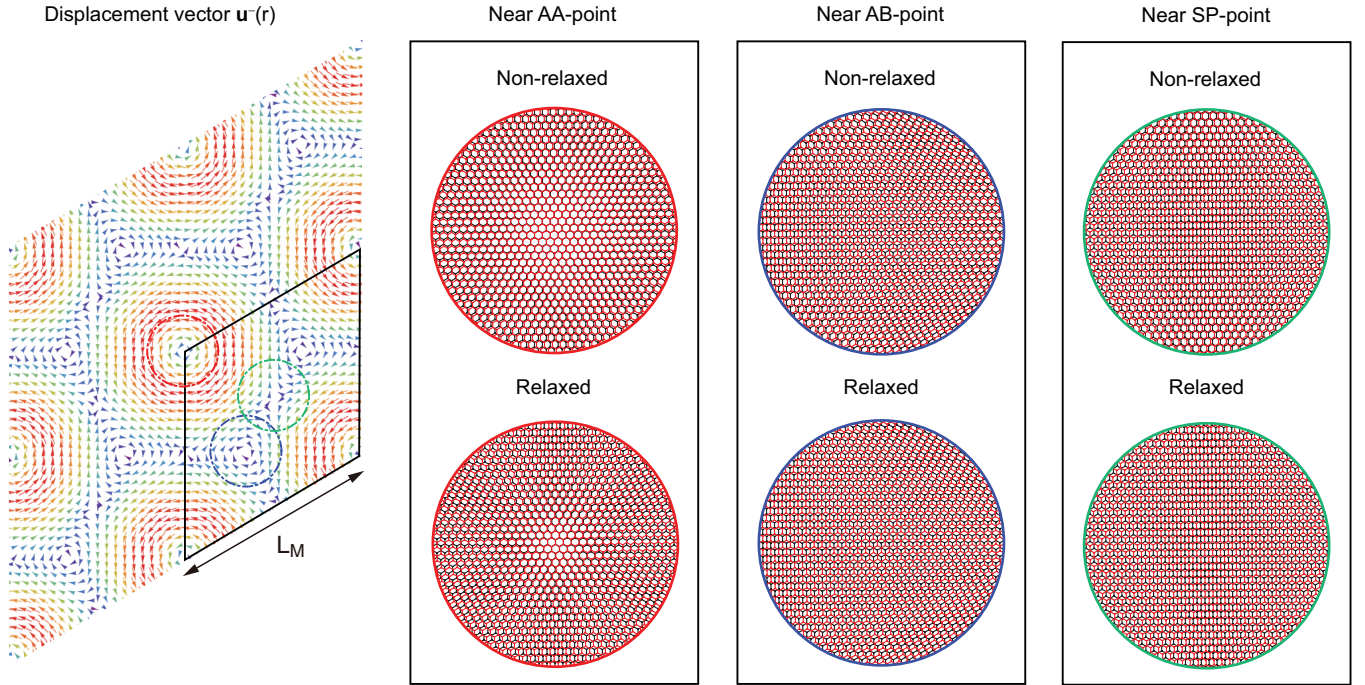
FIG. 7. Outermost panel: Distribution of the displacement vector $\mathbf{u}^-(\mathbf{r})$ in the TBG of $\theta = 1.05°$. Right side panels: Local atomic structure near AA (AB or SP) stacked point before and after the relaxation. The small dashed circles in the center panel indicate the areas where the local structure is sampled.

The present calculation assumed that the relaxed lattice has the same periodicity as in the original TBG before relaxation. However, relaxing this condition may realize a larger supercell structure by distortion of the domain shape, while we expect that the basic properties, such as the formation and AB/BA domains and the width of the domain wall, are well captured in the current model. The stability of the relaxed state is also linked to phonon modes in this system and it is an important future problem.

IV. BAND STRUCTURE

To calculate the energy band structures in the presence of the lattice strain, we use the tight-binding method. The Hamiltonian is written as

$$H = -\sum_{i,j} t(\mathbf{R}_i - \mathbf{R}_j)|\mathbf{R}_i\rangle\langle\mathbf{R}_j| + \text{H.c.}, \qquad (36)$$

where $\mathbf{R}_i$ is the atomic coordinate, $|\mathbf{R}_i\rangle$ is the wave function at site i, and $t(\mathbf{R}_i - \mathbf{R}_j)$ is the transfer integral between atoms i and j. We adopt the Slater-Koster–type formula for the transfer integral [49],

$$-t(\mathbf{d}) = V_{pp\pi}(d)\left[1 - \left(\frac{\mathbf{d}\cdot\mathbf{e}_z}{d}\right)^2\right] + V_{pp\sigma}(d)\left(\frac{\mathbf{d}\cdot\mathbf{e}_z}{d}\right)^2, \qquad (37)$$

$$V_{pp\pi}(d) = V_{pp\pi}^0 \exp\left(-\frac{d - a_0}{r_0}\right), \qquad (38)$$

$$V_{pp\sigma}(d) = V_{pp\sigma}^0 \exp\left(-\frac{d - d_0}{r_0}\right), \qquad (39)$$

where $\mathbf{d} = \mathbf{R}_i - \mathbf{R}_j$ is the distance between two atoms, and $\mathbf{e}_z$ is the unit vector on the z axis. $V_{pp\pi}^0 \approx -2.7$ eV is the transfer integral between nearest-neighbor atoms of monolayer graphene which are located at distance $a_0 = a/\sqrt{3} \approx 0.142$ nm. $V_{pp\sigma}^0 \approx 0.48$ eV is the transfer integral between two nearest vertically aligned atoms. $d_0 \approx 0.334$ nm is the interlayer spacing. The decay length r_0 of transfer integral is chosen at $0.184a$ so that the next-nearest intralayer coupling becomes $0.1V_{pp\pi}^0$ [12,50]. At $d > \sqrt{3}a$, the transfer integral is very small and negligible.

Using the optimized structure obtained in the last section, we specify the lattice position of each single atom in the relaxed TBG, construct the tight-binding Hamiltonian, and calculate the energy bands. Figure 9 compares the electronic band structure of relaxed (black solid lines) and nonrelaxed (red dashed lines) TBGs at several rotation angles. The horizontal axes are labeled by the symmetric points of the Brillouin zone for the moiré superlattice (Fig. 2), and it scales in proportion to $2\pi/L_M$. At $\theta = 2.65°$, we only see a minor difference in accordance with the small change in the lattice structure in Fig. 8(a). A significant deviation is observed below $2°$. The most notable change from the nonrelaxed case is that a band gap opens between the lowest subband near the Dirac point and the first excited subband both in the electron side and the hole side. Figure 10(a) shows the size of gap versus rotation angle θ. The gap is observed in TBGs of $1° \lesssim \theta \lesssim 1.5°$, and the maximum energy width is about 18 meV.

The lattice strain also strongly modifies the band velocity. Figure 10(b) plots the band velocity at the Dirac point as a function of θ for relaxed and nonrelaxed cases. In both cases, the central band at the Dirac point is gradually flattened in decreasing θ, and the Fermi velocity vanishes at a certain
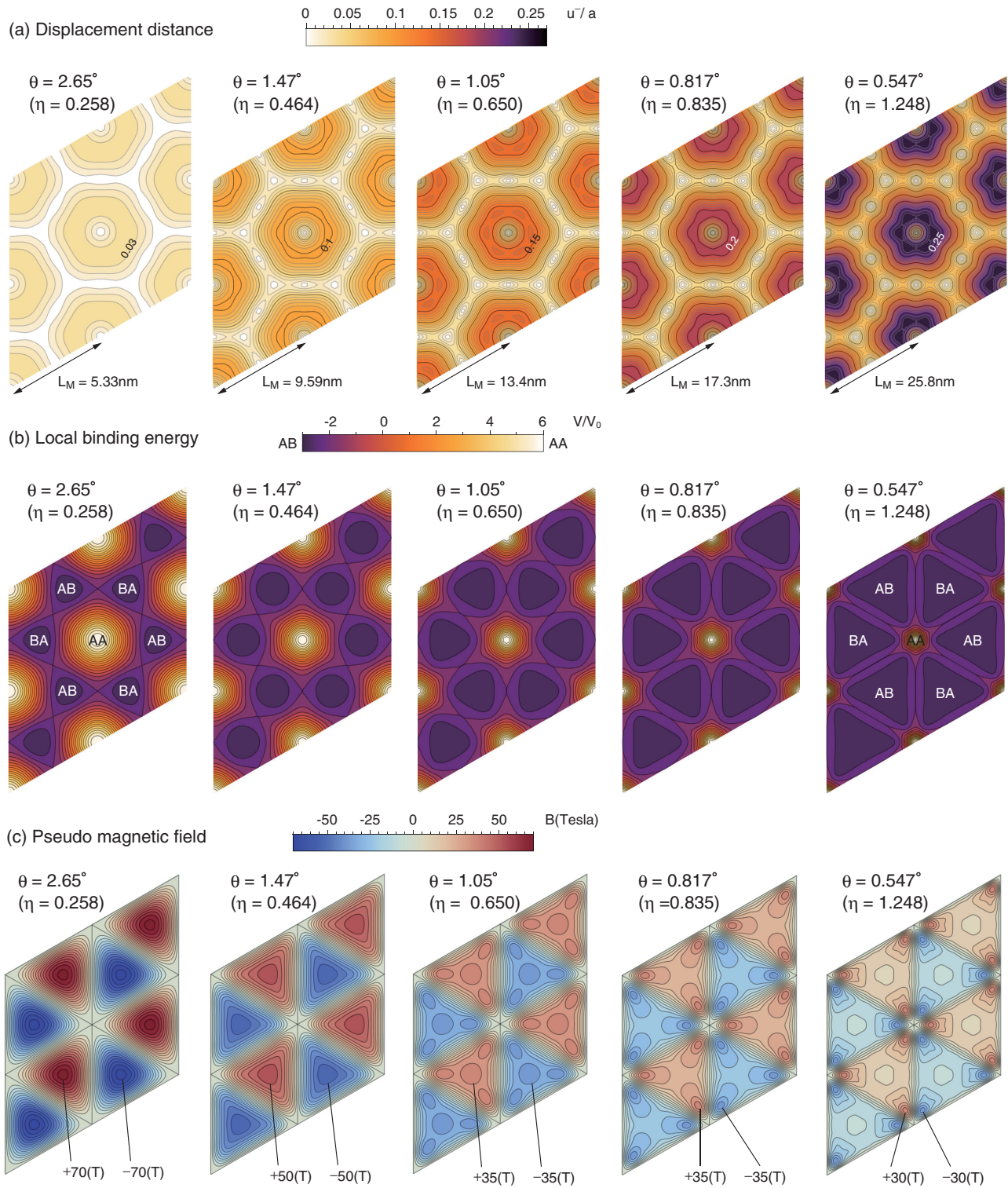
FIG. 8. Two-dimensional maps for (a) absolute value of the displacement vector $\mathbf{u}^-(\mathbf{r})$, (b) the local binding energy $V[\boldsymbol{\delta}(\mathbf{r})]$, and (c) strain-induced pseudomagnetic field $B_{\mathrm{eff}}(\mathbf{r})$, calculated for TBGs with various rotation angles.

angle [15,48]. We find that the band flattening is a little slower in the relaxed case, i.e., at the same angle, the bandwidth is larger in the relaxed TBG than in its nonrelaxed counterpart, so that the critical angle for the vanishing velocity is shifted to the lower rotation angle in the relaxed TBG.

The lattice relaxation affects the electronic structure in two different ways, by a change of interlayer Hamiltonian associated with the modified moiré pattern, and also by a change of the intralayer Hamiltonian through distortion of the lattice. The latter is known to be described by the pseudomagnetic field in the effective mass Dirac Hamiltonian
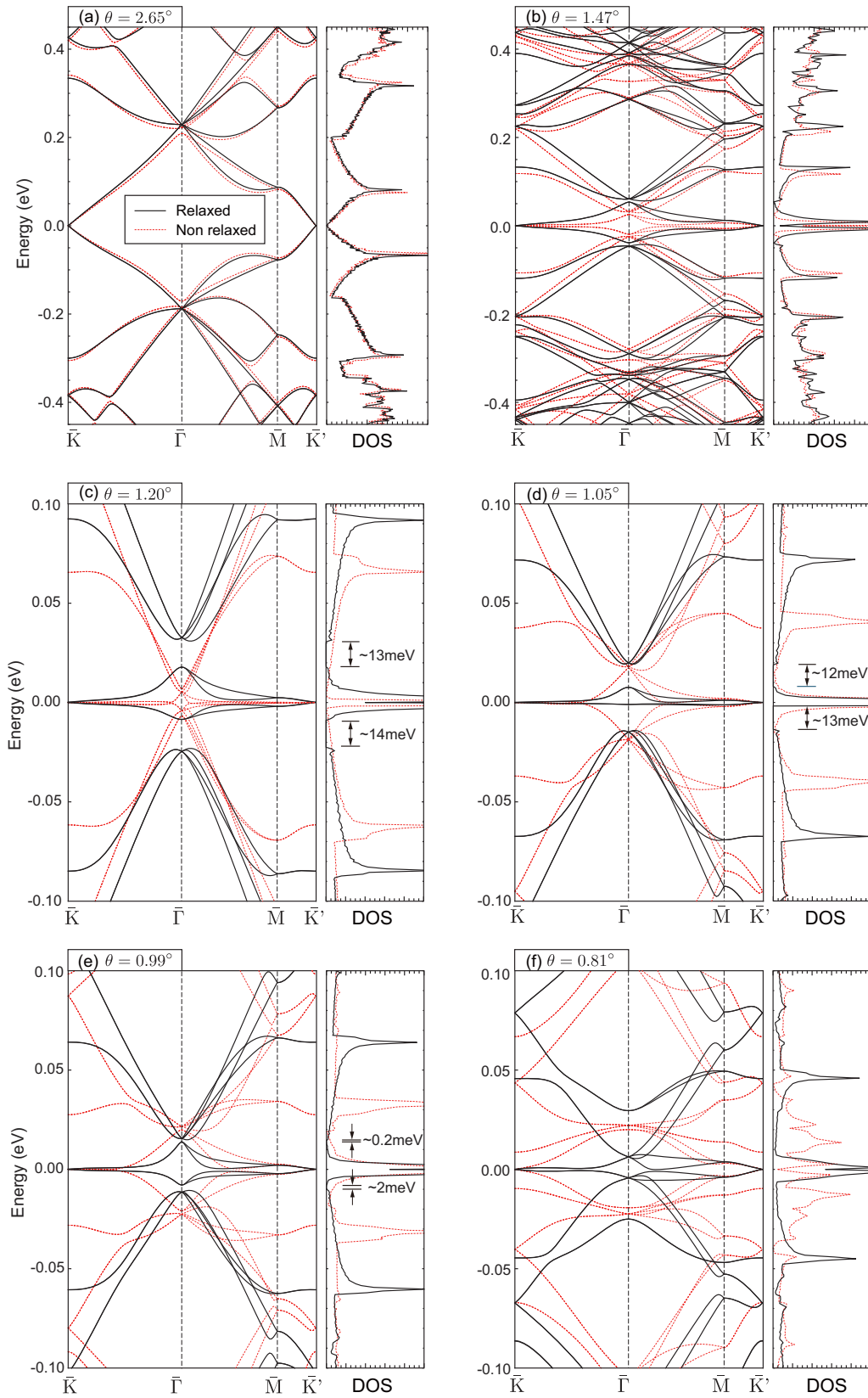
FIG. 9. Band structure and density of state of relaxed (black solid lines) and nonrelaxed (red dashed lines) TBGs at various rotation angles. The energy gap is indicated by a pair of arrows in the DOS panel.
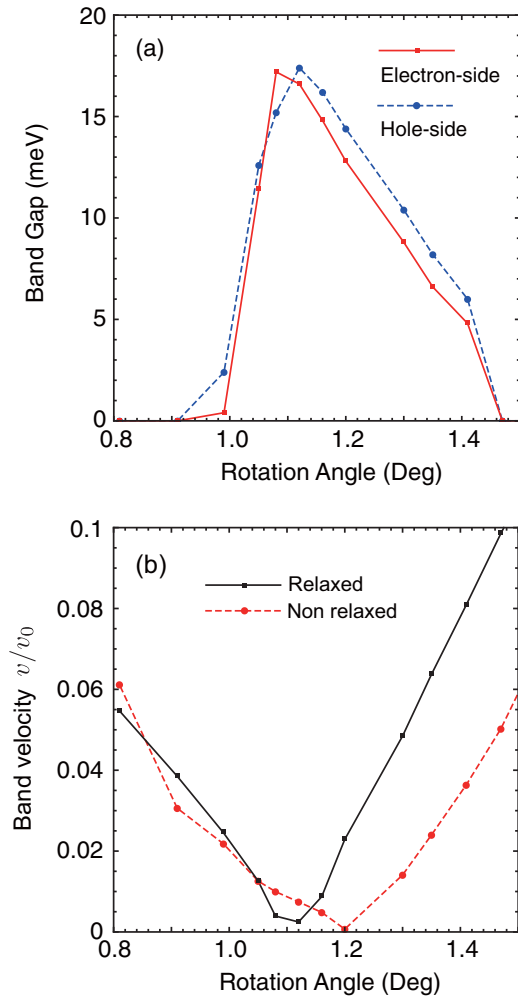
FIG. 10. (a) Band gap between the lowest band and the first excited bands in the electron side (red solid line) and in the hole side (blue dashed), in relaxed TBGs against the rotation angle. (b) Band velocity at K point as a function of θ for relaxed (black solid) and nonrelaxed (red dashed) TBGs.

[45–47]. The vector potential for the pseudomagnetic field on layer $l(=1,2)$ is given by [45–47]

$$A_x^{(l)} = \frac{3}{4} \frac{\beta \gamma_0}{ev} \left[u_{xx}^{(l)} - u_{yy}^{(l)} \right], \tag{40}$$

$$A_y^{(l)} = \frac{3}{4} \frac{\beta \gamma_0}{ev} \left[-2u_{xy}^{(l)} \right], \tag{41}$$

where $\gamma_0 = t(a_0)$ is the nearest-neighbor transfer energy of intrinsic graphene, $v = (\sqrt{3}/2)a\gamma_0$ is the band velocity of the Dirac cone, and

$$\beta = -\left. \frac{d \ln t(d)}{d \ln d} \right|_{d=a_0}. \tag{42}$$

In the present model Eq. (37), we have $\beta = a_0/r_0 \approx 3.14$. The pseudomagnetic field is given by $B_{\mathrm{eff}}^{(l)} = [\nabla \times \mathbf{A}^{(l)}]_z$.

Figure 8(c) shows the distribution of the pseudomagnetic field on layer 1 for several TBGs. The field direction is opposite between layers 1 and 2, because $\mathbf{u}^{(1)} = -\mathbf{u}^{(2)}$. We observe a triangular pattern with positive and negative field domains, which are centered at the AB and BA stacking

regions, respectively. The field amplitude is huge, but it does not necessarily result in a strong effect on the electronic structure, since it is rapidly oscillating in space with nanometer scale. The pseudomagnetic field enters in the Hamiltonian as a form of evA with the pseudovector potential A. When the field spatially modulates with the wavelength L_{M}, the associated matrix element opens a band gap at the energy $E \approx \hbar v/L_{\mathrm{M}}$ measured from the Dirac point. Therefore the effect of the pseudofield significantly affects the band structure when $evA >\approx \hbar v/L_{\mathrm{M}}$, while otherwise it is just perturbative. Now the scale of evA is roughly estimated as

$$evA \approx \beta \gamma_0 u_{ij} \approx 2\beta \gamma_0 \frac{u}{a} \sin \frac{\theta}{2}, \tag{43}$$

where the strain tensor u_{ij} is estimated about $u/L_{\mathrm{M}} = 2(u/a)\sin(\theta/2)$, considering the displacement field $\mathbf{u}$ is modulating with the moiré wavelength $\sim 1/L_{\mathrm{M}}$. The typical scale of u/a can be read from Fig. 8(a). For $\theta = 2.65°$, for example, $u/a \approx 0.03$ gives $evA \approx 10$ meV, and it is much smaller than $\hbar v/L_{\mathrm{M}} \approx 180$ meV. So the effect of evA is perturbative, and this is consistent with a small change in the band structure observed in Fig. 9(a). For $\theta = 1.05°$, on the other hand, $evA \approx 30$ meV is comparable with $\hbar v/L_{\mathrm{M}} \approx 50$ meV, so the pseudofield plays a significant role in the modification of the low-energy bands.

The present model takes account of only the in-plane components of the lattice distortion, as it is aimed to describe the domain formation within the simplest theoretical framework. Inclusion of the out-of-plane motion is known to give rise to a corrugation in the perpendicular direction [26–29], where the interlayer spacing modulates by 10%. In a small-angle TBG less than 2°, in particular, the detailed computational study showed that the interlayer spacing is largest only near the AA spot, while it is almost flat otherwise [27,28]. The corrugation is small even at the AB/BA domain boundary, presumably because it is a shear boundary with no tensile strain, and also the optimized interlayer spacing does not strongly depend on the stacking structure around there. A rough estimation of the corrugation effect on the electronic structure is possible by using the effective continuum model. In the low-angle TBG with no lattice distortion, the interlayer interaction is expressed by a specific matrix form which only depends on a single amplitude parameter $\tilde{t}(K)$ [51,52]. Here $\tilde{t}(q)$ is the Fourier transform of $t(\mathbf{R}_i - \mathbf{R}_j)$ in Eq. (36), and $K = 4\pi/(3a)$ is the wave vector of the K point. We can incorporate the out-of-plane distortion into the effective model by including the position dependence of the interlayer distance in $t(\mathbf{R}_i - \mathbf{R}_j)$, and it results in a change of the amplitude parameter $\tilde{t}(K)$. Therefore the effect of the corrugation is incorporated as renormalization of the interlayer coupling strength. By assuming the modulation in the interlayer spacing predicted in previous works ($\sim 10\%$) [26–29], the change of $\tilde{t}(K)$ is estimated about the order of 10%, so we expect the band structure would not be changed beyond that scale. The detailed band calculation, fully including both in-plane and out-of-plane distortion, is left for future work.

V. CONCLUSION

We have developed an effective theory to calculate the spontaneous relaxation in TBG and studied the atomic and
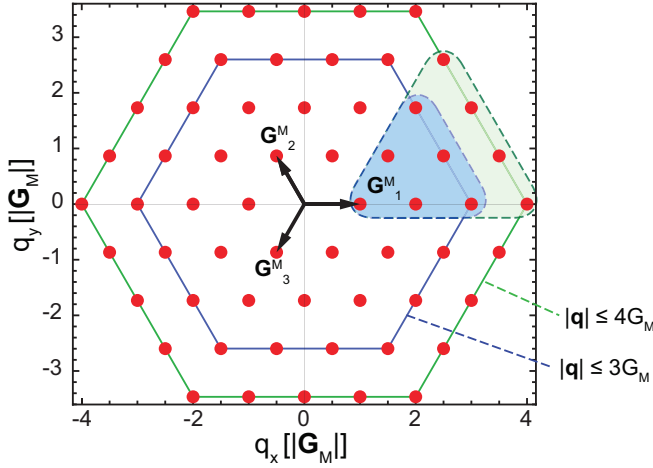
FIG. 11. Schematic of all **q** points within radius $4G_M$ in reciprocal space. The independent **q** points when $\theta > 1°(\theta < 1°)$ are marked by blue (green) triangles.

electronic structures. In rotation angle larger than $2°$, the lattice is hardly deformed and so the effect on the electronic structure is minimal, while in smaller rotation angles below $2°$, the lattice is significantly modified to form a AB/BA triangular domain structure. The electronic band structure is then strongly modified where a band gap of up to $20\,\mathrm{meV}$ opens above and below the lowest band. The lattice deformation also significantly relaxes the band flattening observed in the nonrelaxed case, and it lowers the critical angle at which the Fermi velocity vanishes.

Actually a recent experiment observed an insulating gap of about $50\,\mathrm{meV}$ at the superlattice subband edges in TBG with $\theta \approx 1.8°$ [23]. This seems qualitatively consistent with the present result, although $1.8°$ is out of the gap-opening range in our model calculation, and also $50\,\mathrm{meV}$ is a bit too large compared to the typical gap width obtained here. As we

see in the present work, however, the lattice relaxation and the electronic structure sensitively depend on the parameter η, and it might be possible that the real system could have a greater interlayer interaction, allowing a greater gap and a wider range in the rotation angle for gap opening. It is also conceivable that the gap could be enhanced when the Fermi energy is right at the superlattice gap position, while the doping effect is not considered in the present study. We leave the further quantitative arguments for a future problem.

APPENDIX: NUMERICAL RESULT OF $\mathbf{u}_{\mathbf{q}}^{-}$

The interlayer distortion $\mathbf{u}^{-}(\mathbf{r})$ is Fourier transformed as Eq. (31) with discrete wave numbers $\mathbf{q} = m_1 \mathbf{G}_1^M + m_2 \mathbf{G}_2^M$. The number of relevant harmonics **q** is determined by the dimensionless parameter η, where the larger η indicates that higher harmonics need to be included. In this paper, we consider harmonics within radius $|\boldsymbol{q}| \leqslant 3G_M$ for $\theta > 1°$ and $|\boldsymbol{q}| \leqslant 4G_M$ for $\theta < 1°$ where $G_M = |\mathbf{G}_1^M| = |\mathbf{G}_2^M|$. This results in 36 and 60 q points, respectively (Fig. 11). When assuming that the relaxed states preserve the sixfold rotational symmetry, these harmonics are not totally independent but are related by

$$\mathbf{u}_{R_{60°}\mathbf{q}}^{-} = R_{60°}\mathbf{u}_{\mathbf{q}}^{-}, \tag{A1}$$

where $R_{60°}$ is a rotation matrix by $60°$. The number of independent q points when $\theta > 1°$ and $\theta < 1°$ is then 6 and 10, respectively, which is indicated by triangles in Fig. 11.

In Table II, we present the numerically obtained Fourier components $\mathbf{u}_{\mathbf{q}}^{-} = (u_{\mathbf{q}}^{x-}, u_{\mathbf{q}}^{y-})$ for the several rotation angles θ considered in the paper.

TABLE II. Fourier components $\mathbf{u}_{\mathbf{q}}^{-} = (u_{\mathbf{q}}^{x-}, u_{\mathbf{q}}^{y-})$ (in units of a) at wave points $\mathbf{q} = m_1 \mathbf{G}_1^M + m_2 \mathbf{G}_2^M$ for the several rotation angles.

(m_1, m_2)	$2.65°$	$1.47°$	$1.20°$	$1.05°$
(1,0)	$(-0.009000, 0.005132)$	$(-0.02432, 0.01404)$	$(-0.03187, 0.01840)$	$(-0.03720, 0.02148)$
(2,0)	$(-0.0001725, 0.00009961)$	$(-0.001429, 0.0008251)$	$(-0.002620, 0.001513)$	$(-0.003773, 0.002178)$
(2,1)	$(-0.0002126, 0)$	$(-0.0014907, 0)$	$(-0.002461, 0)$	$(-0.003240, 0)$
(3,0)	$(-4.506 \times 10^{-6}, 2.601 \times 10^{-6})$	$(-0.0001123, 0.00006483)$	$(-0.0002835, 0.0001637)$	$(-0.0004952, 0.0002859)$
(3,1)	$(-6.753 \times 10^{-6}, 3.067 \times 10^{-6})$	$(-0.0001382, 0.00006650)$	$(-0.0003127, 0.0001529)$	$(-0.0005003, 0.0002456)$
(3,2)	$(-6.753 \times 10^{-6}, -3.067 \times 10^{-6})$	$(-0.0001382, -0.00006650)$	$(-0.0003127, -0.0001529)$	$(-0.0005003, -0.0002456)$

(m_1, m_2)	$0.99°$	$0.817°$	$0.547°$
(1,0)	$(-0.03961, 0.02287)$	$(-0.04673, 0.02698)$	$(-0.05922, 0.03419)$
(2,0)	$(-0.004405, 0.002543)$	$(-0.006739, 0.003891)$	$(-0.01351, 0.007798)$
(2,1)	$(-0.003619, 0)$	$(-0.004695, 0)$	$(-0.005696, 0)$
(3,0)	$(-0.0006304, 0.0003639)$	$(-0.001210, 0.0006987)$	$(-0.003570, 0.002061)$
(3,1)	$(-0.0006178, 0.0002969)$	$(-0.001027, 0.0004798)$	$(-0.002013, 0.0007895)$
(3,2)	$(-0.0006178, -0.0002969)$	$(-0.001027, -0.0004798)$	$(-0.002013, -0.0007895)$
(4,0)	$(-0.0001033, 0.00005964)$	$(-0.0002472, 0.0001427)$	$(-0.001044, 0.0006027)$
(4,1)	$(-0.0001211, 0.00007445)$	$(-0.0002535, 0.0001549)$	$(-0.0007323, 0.0004275)$
(4,2)	$(-0.0001156, 0)$	$(-0.0002341, 0)$	$(-0.0006625, 0)$
(4,3)	$(-0.0001211, -0.00007445)$	$(-0.0002535, -0.0001549)$	$(-0.0007323, -0.0004275)$

[1] C. Berger, Z. Song, X. Li, X. Wu, N. Brown, C. Naud, D. Mayou, T. Li, J. Hass, A. N. Marchenkov *et al.*, Science **312**, 1191 (2006).

[2] J. Hass, R. Feng, J. E. Millan-Otoya, X. Li, M. Sprinkle, P. First, W. A. de Heer, E. H. Conrad, and C. Berger, Phys. Rev. B **75**, 214109 (2007).

[3] J. Hass, F. Varchon, J. E. Millan-Otoya, M. Sprinkle, N. Sharma, W. A. de Heer, C. Berger, P. N. First, L. Magaud, and E. H. Conrad, Phys. Rev. Lett. **100**, 125504 (2008).

[4] G. Li, A. Luican, J. M. B. Lopes dos Santos, A. Neto, A. Reina, J. Kong, and E. Andrei, Nat. Phys. **6**, 109 (2009).

[5] D. L. Miller, K. D. Kubista, G. M. Rutter, M. Ruan, W. A. de Heer, P. N. First, and J. A. Stroscio, Phys. Rev. B **81**, 125427 (2010).

[6] A. Luican, G. Li, A. Reina, J. Kong, R. R. Nair, K. S. Novoselov, A. K. Geim, and E. Y. Andrei, Phys. Rev. Lett. **106**, 126802 (2011).

[7] W. A. De Heer, C. Berger, X. Wu, M. Sprinkle, Y. Hu, M. Ruan, J. A. Stroscio, P. N. First, R. Haddon, B. Piot *et al.*, J. Phys. D: Appl. Phys. **43**, 374007 (2010).

[8] L. Wang, I. Meric, P. Huang, Q. Gao, Y. Gao, H. Tran, T. Taniguchi, K. Watanabe, L. Campos, D. Muller *et al.*, Science **342**, 614 (2013).

[9] Z. Tan, J. Yin, C. Chen, H. Wang, L. Lin, L. Sun, J. Wu, X. Sun, H. Yang, Y. Chen *et al.*, ACS Nano **10**, 6725 (2016).

[10] J. M. B. Lopes dos Santos, N. M. R. Peres, and A. H. Castro Neto, Phys. Rev. Lett. **99**, 256802 (2007).

[11] E. Mele, Phys. Rev. B **81**, 161405 (2010).

[12] G. Trambly de Laissardière, D. Mayou, and L. Magaud, Nano Lett. **10**, 804 (2010).

[13] S. Shallcross, S. Sharma, E. Kandelaki, and O. A. Pankratov, Phys. Rev. B **81**, 165105 (2010).

[14] E. Suárez Morell, J. D. Correa, P. Vargas, M. Pacheco, and Z. Barticevic, Phys. Rev. B **82**, 121407 (2010).

[15] R. Bistritzer and A. MacDonald, Proc. Natl. Acad. Sci. USA **108**, 12233 (2011).

[16] M. Kindermann and P. N. First, Phys. Rev. B **83**, 045425 (2011).

[17] L. Xian, S. Barraza-Lopez, and M. Y. Chou, Phys. Rev. B **84**, 075425 (2011).

[18] J. M. B. Lopes dos Santos, N. M. R. Peres, and A. H. Castro Neto, Phys. Rev. B **86**, 155449 (2012).

[19] P. Moon and M. Koshino, Phys. Rev. B **87**, 205404 (2013).

[20] P. Moon and M. Koshino, Phys. Rev. B **85**, 195458 (2012).

[21] R. Bistritzer and A. H. MacDonald, Phys. Rev. B **84**, 035440 (2011).

[22] Y. Kim, P. Herlinger, P. Moon, M. Koshino, T. Taniguchi, K. Watanabe, and J. H. Smet, Nano Lett. **16**, 5053 (2016).

[23] Y. Cao, J.Y. Luo, V. Fatemi, S. Fang, J.D. Sanchez-Yamagishi, K. Watanabe, T. Taniguchi, E. Kaxiras, and P. Jarillo-Herrero, Phys. Rev. Lett. **117**, 116804 (2016).

[24] K. Kim, A. DaSilva, S. Huang, B. Fallahazad, S. Larentis, T. Taniguchi, K. Watanabe, B. J. LeRoy, A. H. MacDonald, and E. Tutuc, Proc. Natl. Acad. Sci. USA **114**, 3364 (2017).

[25] A. M. Popov, I. V. Lebedeva, A. A. Knizhnik, Y. E. Lozovik, and B. V. Potapkin, Phys. Rev. B **84**, 045404 (2011).

[26] K. Uchida, S. Furuya, J.-I. Iwata, and A. Oshiyama, Phys. Rev. B **90**, 155451 (2014).

[27] M. van Wijk, A. Schuring, M. Katsnelson, and A. Fasolino, 2D Mater. **2**, 034010 (2015).

[28] S. Dai, Y. Xiang, and D. J. Srolovitz, Nano Lett. **16**, 5923 (2016).

[29] S. K. Jain, V. Jurivci'c, and G. T. Barkema, 2D Mater. **4**, 015018 (2016).

[30] I. V. Lebedeva, A. A. Knizhnik, A. M. Popov, Y. E. Lozovik, and B. V. Potapkin, Phys. Chem. Chem. Phys. **13**, 5687 (2011).

[31] T. Gould, S. Lebegue, and J. F. Dobson, J. Phys.: Condens. Matter **25**, 445010 (2013).

[32] L. Brown, R. Hovden, P. Huang, M. Wojcik, D. A. Muller, and J. Park, Nano Lett. **12**, 1609 (2012).

[33] J. Lin, W. Fang, W. Zhou, A. R. Lupini, J. C. Idrobo, J. Kong, S. J. Pennycook, and S. T. Pantelides, Nano Lett. **13**, 3262 (2013).

[34] J. S. Alden, A. W. Tsen, P. Y. Huang, R. Hovden, L. Brown, J. Park, D. A. Muller, and P. L. McEuen, Proc. Natl. Acad. Sci. USA **110**, 11256 (2013).

[35] C. Dean, L. Wang, P. Maher, C. Forsythe, F. Ghahari, Y. Gao, J. Katoch, M. Ishigami, P. Moon, M. Koshino *et al.*, Nature (London) **497**, 598 (2013).

[36] L. A. Ponomarenko, R. V. Gorbachev, G. L. Yu, D. C. Elias, R. Jalil, A. A. Patel, A. Mishchenko, A. S. Mayorov, C. R. Woods, J. R. Wallbank *et al.*, Nature (London) **497**, 594 (2013).

[37] B. Hunt, J. Sanchez-Yamagishi, A. Young, M. Yankowitz, B. LeRoy, K. Watanabe, T. Taniguchi, P. Moon, M. Koshino, P. Jarillo-Herrero *et al.*, Science **340**, 1427 (2013).

[38] G. L. Yu, R. V. Gorbachev, J. S. Tu, A. V. Kretinin, Y. Cao, R. Jalil, F. Withers, L. A. Ponomarenko, B. A. Piot, M. Potemski *et al.*, Nat. Phys. **10**, 525 (2014).

[39] X. Chen, J. R. Wallbank, A. A. Patel, M. Mucha-Kruczyński, E. McCann, and V. I. Fal'ko, Phys. Rev. B **89**, 075401 (2014).

[40] P. Moon and M. Koshino, Phys. Rev. B **90**, 155406 (2014).

[41] C. Woods, L. Britnell, A. Eckmann, R. Ma, J. Lu, H. Guo, X. Lin, G. Yu, Y. Cao, R. Gorbachev *et al.*, Nat. Phys. **10**, 451 (2014).

[42] P. San-Jose, A. Gutiérrez-Rubio, M. Sturla, and F. Guinea, Phys. Rev. B **90**, 075428 (2014).

[43] P. San-Jose, A. Gutiérrez-Rubio, M. Sturla, and F. Guinea, Phys. Rev. B **90**, 115152 (2014).

[44] J. Jung, A. M. DaSilva, A. H. MacDonald, and S. Adam, Nat. Commun. **6**, 6308 (2015).

[45] H. Suzuura and T. Ando, Phys. Rev. B **65**, 235412 (2002).

[46] V. M. Pereira and A. H. Castro Neto, Phys. Rev. Lett. **103**, 046801 (2009).

[47] F. Guinea, M. Katsnelson, and A. Geim, Nat. Phys. **6**, 30 (2010).

[48] G. Trambly de Laissardière, D. Mayou, and L. Magaud, Phys. Rev. B **86**, 125413 (2012).

[49] J. Slater and G. Koster, Phys. Rev. **94**, 1498 (1954).

[50] S. Uryu, Phys. Rev. B **69**, 075402 (2004).

[51] M. Koshino, New J. Phys. **17**, 015014 (2015).

[52] M. Koshino, P. Moon, and Y.-W. Son, Phys. Rev. B **91**, 035405 (2015).